THE JOURNAL OF PHYSICAL CHEMISTRY C

Article

Cite This: J. Phys. Chem. C 2017, 121, 23062-23071

pubs.acs.org/JPCC

Near-Electric-Field Tuned Plasmonic Au@SiO_2 and Ag@SiO_2 Nanoparticles for Efficient Utilization in Luminescence Enhancement and Surface-Enhanced Spectroscopy

José Luis Montaño-Priede,[†] Ovidio Peña-Rodríguez,[‡] and Umapada Pal*[,†]

[†]Instituto de Física, Benemérita Universidad Autónoma de Puebla, Apdo. Postal J-48, Puebla, Puebla 72570, Mexico

[‡]Instituto de Fusión Nuclear, Universidad Politécnica de Madrid, José Gutiérrez Abascal 2, E-28006 Madrid, Spain

Supporting Information

ABSTRACT: Application of core−shell plasmonic nanostructures in fluorescence enhancement and surface-enhanced Raman scattering (SERS) strongly depends on their near-field electrodynamical environments. A nonradiative energy transfer takes place between fluorescent molecules and surface plasmon when they are too close. However, for a dielectric shell, the SERS intensity of analytes decreases exponentially beyond 2 nm thickness. Although electromagnetic-field enhancement due to surface plasmon still occurs at longer distances from the metal core, it needs a proper design of the composite nanostructure to exploit this advantage, and an optimal distance between the metal-core and analyte/fluorescent molecule still seems necessary. We analyze, both theoretically and experimentally, the near-electric-field (NEF) distributions in the proximity of the core−shell and shell−medium interfaces of Au@SiO_2 and Ag@SiO_2 core−shell structures immersed in common dispersing media such as air, water, and DMSO to investigate the effects of surrounding medium and particle geometry on them. Through Mie-based theoretical calculations, we demonstrate that the NEF distributions near core−shell and shell−medium interfaces depend not only on the geometrical parameters, but also on the dielectric constant gradient at these interfaces. For each of the dispersion media and a wide range of metal-core radii, we calculate the optimum shell thickness for obtaining the maximum near-field enhancement at the core−shell and shell−medium interfaces, the essential requirements for applying these nanostructures in fluorescence enhancement and SERS. Theoretically obtained results have been qualitatively verified with experiments.

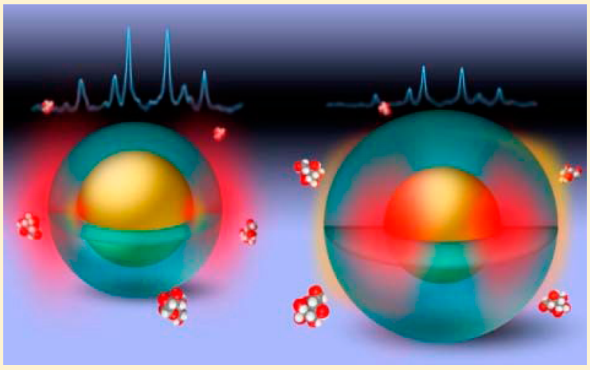

1. INTRODUCTION

Plasmonics has become one of the most attractive fields of modern research due to its vast technological applications.[1] The interaction between conduction electrons of metals and incident electromagnetic (EM) radiation leads to a collective oscillation of these electrons in resonance with the incoming radiation; which is known as localized surface plasmon resonance (LSPR) when it is spatially confined in a metal nanostructure (or a nanocavity).[2] Metal nanoparticles (NPs), particularly those composed of gold or silver, have been widely studied in plasmonic because of their strong LSPR in the visible or near-infrared spectral range, depending on their size, shape, and surrounding media. The LSPR exhibits two important characteristics: the high scattering of the incoming EM radiation at the metal NP surface and the enhancement of electric field close to the metal NP surface (near electric field, NEF).[3] The first of these phenomena can be used to enhance the efficiency of a solar cell,[4] whereas the latter has applications in fluorescence enhancement and SERS.[5−10] For instance, silver NPs have been incorporated in GaN/InGaN light-emitting diodes to increase their emission intensity by coupling the electronic transition of the quantum well to the LSPR of Ag NP.[11] Nevertheless, Ag NPs should be protected with silica or other dielectric layer (shell) to prevent their oxidation during the fabrication and operation of these devices.

In the biomedicine field, Au and silica-coated Au NPs have been tested as labels for thermographic DNA detection.[12] Whereas the target DNA concentrations of ∼100 pM could be detected by bare Au NPs, DNA concentrations as low as 10 pM could be detected when they were coated with silica layers. In fact, gold and silver NPs coated with dielectric layers have been widely utilized during the past few years in photovoltaic devices to increase their efficiency and for enhancing the efficiency of SERS-based molecular detection systems, as in the shell-isolated nanoparticles-enhanced Raman spectroscopy (SHINERS).[8,9,13−17] Utilization of dielectric shells around these plasmonic NPs serves not only to protect them from oxidation or harsh biological media but also as support for

Received: July 26, 2017
Revised: September 22, 2017
Published: September 26, 2017

DOI: 10.1021/acs.jpcc.7b07395
J. Phys. Chem. C 2017, 121, 23062−23071

fluorophores and spacer to control the distance between the metal core and the fluorophores.[18,19] On the contrary, dielectric shells such as silica around Ag or Au NPs increase their chemical stability and biocompatibility for biomedical applications.[20−22] However, it is essential to design metal@dielectric nanostructures of optimum geometry as the application of these metal-core dielectric-shell nanostructures in fluorescence enhancement and SERS depends strongly on the spatial distribution of NEF at the core−shell (C−S) and shell−medium (S−M) interfaces, respectively.

Extinction spectra, obtained either experimentally or calculated theoretically, have been frequently used to evaluate metal-dielectric core−shell plasmonic structures for their fluorescence and SERS utilities.[8,23] However, recently we have demonstrated that this approach fails to provide the exact description of NEF distribution in core−shell NPs.[24] On the experimental front, efforts have been made to optimize the geometrical parameters of core−shell nanostructures to control their NEF distributions for obtaining optimum SERS performance.[8,25,26a,b] It has been demonstrated that Au NPs of 120−135 nm size range with 2 nm thick silica shells provide most intense SERS signal.[9,25,27] However, more intense SERS signal could be detected for Au NPs of smaller sizes (e.g., 55 nm) by reducing silica shell thickness to 1 nm.[26a] Therefore, it is not yet clear how the geometrical parameters of these core−shell plasmonic nanostructures contribute to the NEF distribution around the C−S and S−M interfaces to determine their utility in fluorescence enhancement and SERS-based molecular detection.

To understand the contributions of core size, shell thickness, and the nature of dispersion medium, we calculated the NEF enhancement of plasmonic core@shell NPs consisting of metallic cores and silica shells (Au@SiO_2 and Ag@SiO_2) varying the core radius from 5 to 50 nm and the shell thickness from 0 to 50 nm in common dispersion media, such as air, water, and dimethyl sulfoxide (DMSO). The theoretically predicted results have been verified by performing SERS analysis of Rhodamine 6G dissolved in water and DMSO, utilizing bare Au and Au@SiO_2 NPs (of different geometries) assemblies as SERS substrates.

2. METHODS

2.1. Calculations and Theoretical Considerations. Near electric fields around Au@SiO_2 and Ag@SiO_2 NPs of varied core size and shell thickness were calculated following the theoretical approach based on Mie theory for multilayered spheres, as described in our previous work.[28] In brief, the near electric field can be expressed as the superposition of the inward ($\mathbf{E}_{in}$) and outward ($\mathbf{E}_{out}$) sets of complex spherical eigenvectors

$$\mathbf{E}_{in} = \sum_{n=1}^{\infty} E_n[c_n^{(l)}\mathbf{M}_{o1n}^{(1)} - id_n^{(l)}\mathbf{N}_{e1n}^{(1)}] \quad (1)$$

$$\mathbf{E}_{out} = \sum_{n=1}^{\infty} E_n[ia_n^{(l)}\mathbf{N}_{e1n}^{(3)} - b_n^{(l)}\mathbf{M}_{o1n}^{(3)}] \quad (2)$$

where $E_n = i^n E_0(2n + 1)/n(n + 1)$ and $\mathbf{M}_{o1n}^{(j)}$ and $\mathbf{N}_{e1n}^{(j)}$ (j = 1, 3) are the vector spherical harmonics, and the superscript denotes the kind of Bessel function (explicit expressions can be found elsewhere).[29] For a multilayer sphere, the electric and magnetic fields in each layer (l) region can be calculated by

$$\mathbf{E}_l = \sum_{n=1}^{\infty} E_n[c_n^{(l)}\mathbf{M}_{o1n}^{(1)} - id_n^{(l)}\mathbf{N}_{e1n}^{(1)} + ia_n^{(l)}\mathbf{N}_{e1n}^{(3)} - b_n^{(l)}\mathbf{M}_{o1n}^{(3)}] \quad (3)$$

$$\mathbf{H}_l = \frac{k_l}{\omega\mu}\sum_{n=1}^{\infty} E_n[d_n^{(l)}\mathbf{M}_{e1n}^{(1)} + ic_n^{(l)}\mathbf{N}_{o1n}^{(1)} - ib_n^{(l)}\mathbf{N}_{o1n}^{(3)} - a_n^{(l)}\mathbf{M}_{e1n}^{(3)}] \quad (4)$$

where μ is the magnetic permeability of region l and ω is the angular frequency of the incident wave. The expansion coefficients ($a_n^{(l)}$, $b_n^{(l)}$, $c_n^{(l)}$, and $d_n^{(l)}$) are obtained by matching the tangential components of the electromagnetic field at each interface (see explicit expressions in ref 28).

For these calculations, we considered a metal core (l = 1) of radius (R_C) varying from 5 to 50 nm, covered with a silica shell ($l = L$ = 2) of thickness (t_S) from 0 (bare gold NP) to 50 nm (Figure 1) with spatial resolution of 0.5 nm, surrounded by

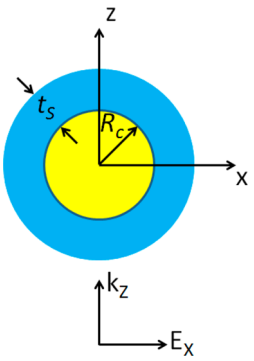

Figure 1. Schematic representation of the composite nanoparticle considered for NEF simulation. R_C is the core radius and t_S the thickness of the shell. The origin of the reference system is located at the center of the nanoparticle. The excitation wave is propagating along the z-direction, with E polarized along the x-direction.

some of the most common dielectric media in which nanoparticles are dispersed; such as air (n_{air} = 1.0002),[30] water (n_{water} = 1.333),[31] and dimethyl sulfoxide (DMSO, n_{DMSO} = 1.4769),[32] whose refractive indices are close to the refractive index of silica.

For the sake of simplicity, the core radius was limited to 50 nm as the maximum of the electric field predominantly corresponds to the dipolar mode for Au/Ag NPs of smaller radius,[24] and the considered size range covers the sizes of commonly fabricated Au NPs.[33] The complex refractive indices of gold and silver were taken from ref 34, and the refractive index of silica was considered fixed n_{silica} = 1.46 for the wavelengths close to the LSPR of Au (500 nm) and Ag (400 nm) NPs.[35] The incident electromagnetic wave is propagating along the z-direction and E-polarized along the x-direction; $\mathbf{E}_i = E_0 \exp[ikz\cos(\theta)]\mathbf{e}_x$, where $k = 2\pi n_M/\lambda$ is the propagation constant, n_M is the refractive index of the transparent medium, and λ is the wavelength of light in vacuum spanning over 300 to 1000 nm, with resolution of 0.5 nm. The results of the NEF for Ag@SiO_2 NPs are presented in the Supporting Information because they are very similar to those obtained for Au@SiO_2 NPs.

2.2. Experimental Section. Spherical Au nanoparticles of ∼50 and ∼75 nm in size and Au@SiO_2 composite nanoparticles of ∼50 nm core radius and ∼10 and ∼15 nm shell thicknesses (Figure 2 and S1, in Supporting Information) were

DOI: 10.1021/acs.jpcc.7b07395
J. Phys. Chem. C 2017, 121, 23062−23071

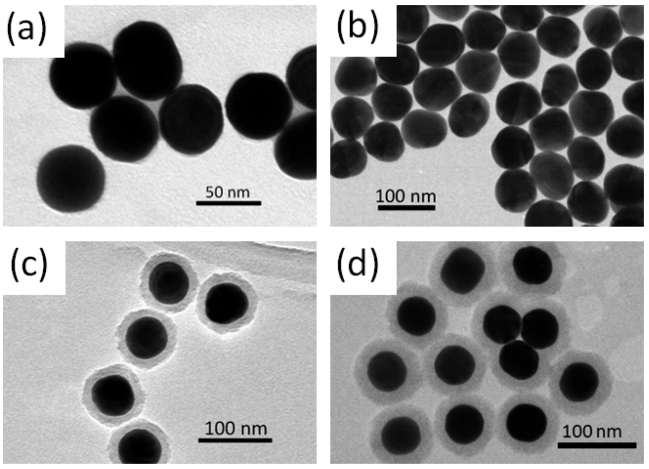

Figure 2. Typical TEM images of Au nanoparticles of (a) 50 in size and (b) 75 nm in size. TEM images of Au@SiO_2 nanoparticles of 50 nm core radius and (c) 10 nm and (d) 15 nm shell thickness (size distribution histograms are shown in Figure S1, Supporting Information).

synthesized following the procedure reported in our previous work.[22] For the synthesis of gold nanoparticles, the materials used were chloroauric acid ($HAuCl_4 \cdot H_2O$, 99.999%), sodium borohydride ($NaBH_4$, 99.99%), L-ascorbic acid (≥99%), cetyltrimethylammonium chloride solution (CTAC, 25 wt % in H_2O), and cetyltrimethylammonium bromide (CTAB, ≥ 99%), all from Sigma-Aldrich. Tetraethyl orthosilicate (TEOS, ≥ 99%) and poly(ethylene glycol)methyl etherthiol (mPEG-SH, av. M_w = 6000) from Sigma-Aldrich, ammonium hydroxide (NH_4OH, aq. sol. 10−35%) from Quimivita, and absolute ethanol (99.9%) from Scharlau were used for silica shell fabrication.

In short, $NaBH_4$ aqueous solution (600 μL, 10 mM) was added to CTAB (100 mM) and $HAuCl_4$ (0.25 mM) aqueous solution (10 mL). Then, aqueous solution of $HAuCl_4$ (2 mL, 0.5 mM) was added to CTAC aqueous solution (22 mL, 18.8 mM) containing ascorbic acid (1.5 mL, 100 mM) and Au cluster solution (50 μL), resulting in Au NPs of ∼10 nm average diameter. Finally, to increase the size of the previously synthesized Au NPs, an aqueous $HAuCl_4$ solution (40 mL, 5 mM) was slowly injected (20 mL/h) to CTAC aqueous solution (200 mM) containing ascorbic acid solution (3.24 mL, 100 mM) and the as-prepared colloid of ∼10 nm Au NPs (150 or 70 μL) to obtain Au NPs of 50 or 75 nm, respectively. The whole synthesis process was performed at room temperature.

For the growth of silica shell, gold nanoparticles of ∼50 nm were functionalized with mPEG-SH and transferred to an ethanol solution.[22] Then, two solutions were prepared separately. The first solution (sol. 1) was prepared by mixing the Au-NP ethanol solution (2.5 mL), deionized water (1.35 mL), and NH_4OH (100 μL) in ethanol (3.75 mL). The second solution (sol. 2) was prepared by adding TEOS (50 μL) to ethanol (7.4 μL). Then, sol. 2 (300 μL for shell thicknesses of ∼10 nm or 400 μL for shell thicknesses of ∼15 nm) was added to sol. 1. The reaction mixture was kept under ultrasonic treatment (37 kHz, 80 W) for 2 h to increase the chemical stability of the silica shell and avoid NPs agglomeration,[22] maintaining the temperature of the water bath fixed (20 °C). Finally, the solution was centrifuged twice and the product was redispersed in ethanol.

SERS substrates were fabricated by assembling the fabricated Au and Au@SiO_2 NPs over silicon substrates through drop-casing their colloidal solutions. The substrates were dried at

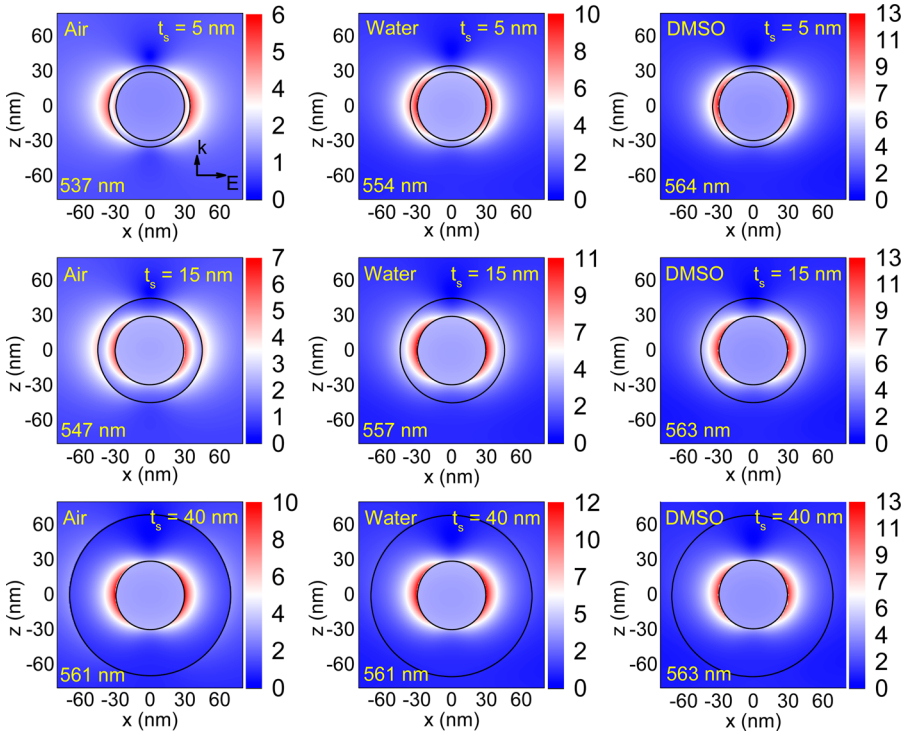

Figure 3. Electric-field enhancement ($|\mathbf{E}|/|\mathbf{E}_0|$) color maps in the *xz*-plane (at *y* = 0 nm) of an Au@SiO_2 NP of a fixed core radius (R_C = 30 nm) and different shell thicknesses (t_S = 5, 15, and 40 nm) surrounded by air, water, and DMSO. Excitation wavelengths correspond to the λ_{NEF} of the corresponding structures.

DOI: 10.1021/acs.jpcc.7b07395
J. Phys. Chem. C 2017, 121, 23062−23071

room temperature for 1 day. The substrates fabricated by the assembly of bare Au NPs of ∼50 and ∼75 nm diameters were labeled as Au_50 and Au_75, respectively. On the contrary, the substrates fabricated by assembling the Au@SiO_2 NPs with shell thickness ∼10 and ∼15 nm were designated as Au@SiO_2_10 and Au@SiO_2_15, respectively. The as-prepared SERS substrates were air-annealed (300 °C, 0.5 h) in an open tube furnace to ensure the desorption of the thiol from the nanoparticle surface.[36] Desorption of thiol from the SERS substrate was verified by the Raman spectra of the substrate before and after thermal treatment (Figure S2, Supporting Information). The fabricated SERS substrates were tested for Raman signal enhancement of rhodamine 6G (R6G, Sigma-Aldrich) dissolved in water and DMSO in 1 mM concentration. A LabRAM HR Raman spectrometer (Horiba Jobin Yvon) with Olympus BX41 microscope (10× objective) and 632.8 nm He−Ne Laser beam (6.28 mW) was used for recording the Raman and SERS spectra of the R6G solutions (1 drop = 10 μL) over the SERS substrates.

3. RESULTS AND DISCUSSION

In Figure 3, near-electric-field enhancements ($|\mathbf{E}|/|\mathbf{E}_0|$) are plotted for an Au@$SiO_2$ core−shell NP with fixed core radius, R_C = 30 nm, and shell thicknesses of 5, 10, and 40 nm, surrounded by three different media, air, water, and DMSO, to show the variations of the electric field as a function of shell thickness and surrounding medium. The NEF enhancements are plotted in the xz-plane (at y = 0 nm), the plane formed by the incident wave vector ($\boldsymbol{k}_z$) and the E-polarized unit vector ($\boldsymbol{e}_x$), where the maximum electric field of gold NPs is located. The near-field enhancement of Au@SiO_2 NPs corresponds to the dipolar mode,[24] as can be seen in the calculated $|\mathbf{E}|/|\mathbf{E}_0|$ spectra at the C−S (first row of Figure S3, Supporting Information) and S−M (first row of Figure S3, Supporting Information) interfaces. In the case of an Ag@SiO_2 NP (second row of Figure S3 for $|\mathbf{E}|/|\mathbf{E}_0|$ at C−S interface and second row of Figure S4 for $|\mathbf{E}|/|\mathbf{E}_0|$ at S−M interface, Supporting Information), multiple maxima of NEF as a function of excitation wavelength are well-defined, where each maximum is associated with a particular polar mode (dipole, quadrupole, and octupole modes).[24] However, we will only focus on the NEF maxima associated with the dipolar mode to compare the results with those of Au@SiO_2 NPs.

As can be seen in Figure 3, the maximum intensity of NEF for an Au@SiO_2 NP excited with appropriate wavelength (λ_{NEF}) is 6 to 12 times higher than that of the incident field. The intensity of NEF maximum increases along with a red shift of the resonant wavelength on increasing either n_M or t_S. Similar results have been obtained for an Ag@SiO_2 NP (Figure S5, Supporting Information). The increase in the NEF for higher n_M might be due to the higher intensity of the light transmitted through the silica shell, that is, lower reflection from the silica surface due to smaller difference between the refractive indexes of the medium n_M and the silica shell n_{silica};[37] the condition that favors more electrons of the metallic core to resonate. The red shift of λ_{NEF} on increasing n_M is a well known phenomenon, easily described by the Drude model for metallic particles in which the surface resonant wavelength is proportional to n_M.[38,39] On the contrary, the effective permittivity (or effective refractive index) of the medium surrounding the core, which is composed of silica and air in the present case, increases when the thickness of the silica shell increases, following the Bruggeman effective medium theory for composite materials,[40] red-shifting the NEF.[15,41]

The NEF of each NP configuration has two pairs of local maximum values, one pair at the C−S interface and the other at the S−M interface along the E-polarized direction (Figure 3 and Figure S6 of the Supporting Information). The electric-field maxima at the C−S interface are due to the localized plasmon at metal surface, as described by Willets and van Duyne[7] through the quasi-static approximation for $R_C/\lambda < 0.1$. On the contrary, the maxima at the S−M interface are due to the mismatch of wave impedances in the shell and the surrounding medium, which generates fixed charge density at this interface induced by both the polarization of the incident field and the electric field of the dipolar core plasmon, manifesting as nonpropagating evanescent waves at the S−M interface.[42]

As can be seen from the first and second columns of the plots of Figure 3 (corresponding to air and water media), the maximum electric field at the S−M interface (E_{S-MI}) is prominent when the refractive index of the surrounding medium is smaller than the refractive index of silica shell. Nevertheless, the electric field at the S−M interface fades away on increasing n_M, making the maximum electric field at the C−S interface (E_{C-SI}) stronger, as shown in the third column of Figure 3 (see also first row of Figure S6, Supporting Information). The E_{S-MI} becomes negligible when the optical impedance mismatch between the shell and the medium approaches to zero, that is, when S−M interface becomes optically invisible.[37] The increase in E_{C-SI} with the increase in n_M (reduced impedance mismatch) is basically due to the reduction in light reflection at the S−M interface and hence the increase in SPR intensity due to brighter illumination of the metal core and the increase in effective refractive index (Bruggeman effective medium theory) of the medium surrounding it, as previously described. For silver, E_{C-SI} decreases on increasing n_M (second row of Figure S6, Supporting Information) as the core dipolar plasmon intensity for silver NPs of bigger core radius (e.g., R_C = 30 nm) reduces on the increase in effective refractive index of surrounding medium (second row of Figures S3 and S4, Supporting Information).[24] Instead, the contribution of the higher plasmon modes (quadrupolar and octupolar modes) to E_{C-SI} intensity increases for bigger core radius (second row of Figures S3 and S4, Supporting Information). Nevertheless, E_{S-MI} also becomes negligible, as for Au@SiO_2 NP, when n_M approaches n_{silica} (second row of Figure S6, Supporting Information). On the contrary, E_{C-SI} decreases with the increase in shell thickness (Figure S3, Supporting Information) as the electric field produced by the metal-core plasmon decays exponentially from the C−S to S−M interface.[24]

As expected, for most of the configurations of Au@SiO_2 NP presented in Figure 3, E_{C-SI} is higher than E_{S-MI} (Figure S6, Supporting Information), as the electric field at the former interface is governed by the radiative emission from oscillating electrons of the metallic core at λ_{NEF}.[43] On the contrary, the E_{S-MI} can be more intense than E_{C-SI} for thinner shells, such as for the case of Au@SiO_2 NP with t_S = 5 nm in air (the top color map of the left column, Figure 3) to satisfy the boundary condition for the continuity of electric field at the S−M interface. The boundary condition for the normal components of the electric displacement vectors ($\mathbf{D}_{S,M} = \varepsilon_{S,M}\mathbf{E}_{S,M}$, where $\varepsilon_S = n_S^2$ and $\varepsilon_M = n_M^2$ are the dielectric constants of the shell and

DOI: 10.1021/acs.jpcc.7b07395
J. Phys. Chem. C 2017, 121, 23062−23071

surrounding medium, respectively) at the S−M interface that must be satisfied is[29]

$$\boldsymbol{e}_n \cdot (\mathbf{D}_S - \mathbf{D}_M) = \rho \quad (5)$$

where ρ is the surface charge (free) density at the interface and $\boldsymbol{e}_n$ is the normal unit vector. In the present case, $\rho = 0$ because both of the materials, the shell and the surrounding medium, are of dielectric nature, and $\boldsymbol{e}_n$ is parallel to the surface vector due to the spherical symmetry of the interface. Now, substituting the expressions for $\mathbf{D}_S$ and $\mathbf{D}_M$ in eq 5, we obtain

$$\varepsilon_S E_S = \varepsilon_M E_M \quad (6)$$

or

$$\varepsilon_S/\varepsilon_M = E_M/E_S \quad (7)$$

Thus the electric field intensity in the surrounding medium (E_M) must be higher than inside the shell (E_S) to satisfy the equality of eq 7 at the interface because $\varepsilon_S > \varepsilon_M$. Therefore, the maximum of the electric field at the C−S interface is required to be modulated for thinner silica shells in such a way that the intensity of the decayed electric field near the S−M interface at the shell side must be lower than the maximum of the electric field at the medium side of the S−M interface (E_{S-M}). As the shell thickness increases, this requirement becomes less trivial as the electric field due to the metal core (E_{C-S}) decays exponentially with distance,[44] and its intensity becomes very low at the S−M interface due to larger separation between C−S and S−M interfaces. When the dielectric constants of the shell and the surrounding medium are equal or very close ($\varepsilon_S \approx \varepsilon_M$), the difference between E_M and E_S becomes negligible ($E_M \approx E_S$, eq 7), and the distribution of the electric field around the S−M interface becomes uniform (not distinguishable).

Now, as both E_{C-SI} and E_{S-MI} can be tuned by controlling the geometrical parameters of these plasmonic core−shell structures and their dispersion medium, we computed the ratio between the NEF at the C−S interface and the S−M interface (E_{C-SI}/E_{S-MI}) as a function of R_C, t_S, and n_M to determine for which configurations of Au@SiO_2 the E_{C-SI} is higher than E_{S-MI} and vice versa (Figure 4, and Figure S7 for Ag@SiO_2, Supporting Information). The intention is to design spherical plasmonic NPs of optimum dimensions for utilization in specific systems, such as surface-enhanced spectroscopy (SES) and plasmon-enhanced fluorescence (PEF), prior to their synthesis. For instance, the ratio E_{C-SI}/E_{S-MI} less than one indicates that the NEF at the S−M interface is greater than that at the C−S interface, as in the aforementioned example of the Au NP with t_S= 5 nm in air.

These nanoparticles are suitable for use as SERS substrates for detecting analytes that are located near the S-M interface, as the Raman signal of the analytes would be more intense in comparison with the signal obtained using NPs with thicker silica shells. On the contrary, if we are interested in enhancing the fluorescence of dyes located near the metal core (inside the silica matrix), we can design an Au@SiO_2 NP (e.g., modifying the silica shell thickness) in which NEF at the C−S interface is greater than that at the C−S interface ($E_{C-SI}/E_{S-MI} > 1$) for obtaining optimal fluorescence enhancement (e.g., an Au@SiO_2 NP with R_C = 30 nm and t_S = 40 nm, Figure 3).

For the nanoparticles in air (Figure 4a), we determine that for a particular core radius there is a specific shell thickness for which the ratio E_{C-SI}/E_{S-MI} is equal to one; that is, the intensity of E_{C-SI} is equal to E_{S-MI} (white line in Figure 4a). The linear relation between Au core radius and silica shell thickness for

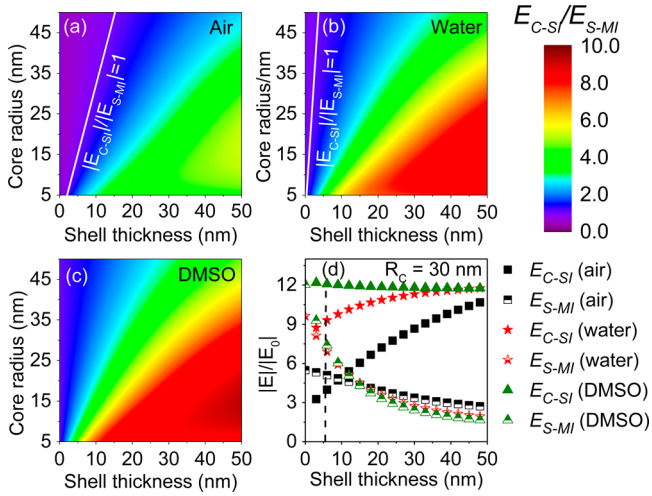

Figure 4. Color maps of E_{C-SI}/E_{S-MI} as a function of core radius (y-axis) and shell thickness (x-axis) for an Au@SiO_2 NP dispersed in (a) air, (b) water, and (c) DMSO. The white lines indicate the geometrical configurations for which E_{C-SI}/E_{S-MI} = 1. The ratio E_{C-SI}/E_{S-MI} is less than one on the left of this line and more than one on the right side. (d) Graphical presentation of the variation of E_{C-SI} and E_{S-MI} for an Au@SiO_2 NP (R_C = 30 nm) dispersed in air, water, and DMSO as a function of the shell thickness. The NEF enhancements ($|E|/|E_0|$) at the interfaces were estimated using the maximum of electric fields at those interfaces for the excitation wavelengths corresponding to the λ_{NEF} of the corresponding structures.

which $E_{C-SI} = E_{S-MI}$ (in air medium) can be expressed as (eq S1 for Ag@SiO_2, Supporting Information)

$$t_S = 0.3R_C + 0.4 \text{ (nm)} \quad (8)$$

As can be seen from Figure 4a, the silica thicknesses for the considered range of core radius for which $E_{C-SI} < E_{S-MI}$ (E_{S-MI} could be up to two times more intense than E_{C-SI}) remain at the left side of the white line, where the silica shells are thin. These Au@SiO_2 NPs with thin shells are most suitable for their utilization in surface-enhanced spectroscopies and plasmon-enhanced fluorescence, where the analytes (for SES) or the fluorophores (for PEF) are located (adsorbed or anchored) near the S−M interface. In fact, Au NPs covered with thin SiO_2 shells have been utilized for SERS to characterize biological structures such as yeast cells, determining the main components of their cell walls.[9] On the contrary, Kochuveedu et al.[45] have utilized Au@SiO_2 particles of 15 nm core radius and 5, 10, and 12 nm shell thicknesses to decorate with CdSe quantum dots (QDs) for the study of plasmon-induced fluorescence enhancement of the CdSe QDs. The maximum fluorescence enhancement observed by them (~65% with respect to bare CdSe QDs) was for silica shell thickness of 10 nm. A reduction of shell thickness was observed to diminish the enhancement (~44% with respect to bare CdSe QDs) due to energy transfer between the QDs and the Au core. The fluorescence enhancement diminished further (~16% with respect to bare CdSe QDs) for the shell thickness higher than 10 nm due to larger separation between the Au core and the CdSe QDs.

Our theoretically predicted effects of shell thickness over NEF distribution in the core−shell structures were qualitatively verified by measuring the Raman spectra of Rhodamine 6G (R6G) over the substrates fabricated by dispersing Au@SiO_2 particles of 50 nm core diameter and silica shell thicknesses of

DOI: 10.1021/acs.jpcc.7b07395
J. Phys. Chem. C 2017, 121, 23062−23071

10 and 15 nm (Au@SiO_2_10 and Au@SiO_2_15 substrates, respectively). For that, first the spherical Au nanoparticles of desired sizes were fabricated by successive seed-mediated growth process[22] and then covered by SiO_2 shells of desired thicknesses using ultrasound assisted Stöber method[22] (Figure 2).

The bands revealed in the Raman spectra (Figure 5) are associated with the vibrational modes of R6G in aqueous solution (Table 1). Estimated integral intensity of each spectrum in the 1100−1700 cm^{-1} range (shown in parentheses next to the label in Figure 5) was used to compare the signal enhancement by the fabricated SERS substrates. It can be noticed that whereas the Raman signal enhancement for the substrate $I_{Au@SiO_2\_10}$ with respect to bare Si substrate ($I_{Au@SiO_2\_10}/I_{Si}$) is ≅ 3.8, the same for the $I_{Au@SiO_2\_15}$ substrate ($I_{Au@SiO_2\_15}/I_{Si}$) is ≅ 2.4, indicating a reduction of signal enhancement for thicker silica shell due to the reduction of $|E_{S-MI}|$.

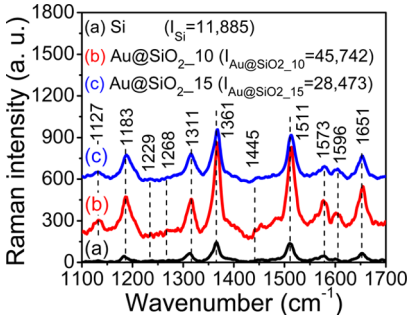

Figure 5. Raman spectra of R6G (1 mM) in aqueous solution recorded over silicon (curve a), Au@SiO_2_10 (curve b), and Au@SiO_2_15 (curve c) substrates. Labeled bands correspond to the vibrational modes of R6G (see Table 1).

Table 1. Position and Assignment of the Observed Raman Bands of R6G Dissolved in Water and DMSO

positions of Raman bands for R6G in water (cm^{-1})	positions of Raman bands for R6G in DMSO (cm^{-1})	band assignment
1127	1127	C−H in plane bending[46]
1183	1183	C−C stretching[47]
1229	1233	phenyl ring[48]
1268	1270	C−O−C stretching[46]
1311	1315	aromatic C−C stretching[47]
1361	1367	aromatic C−C stretching[46,47]
1445	1445	phenyl ring[48]
1511	1514	aromatic C−C stretching[46,47]
1573	1573	aromatic C−C stretching[46]
1596	1596	xantene core[48]
1651	1653	aromatic C−C stretching[46,47]

For the applications in which fluorophores or dyes are located inside silica matrix (shell) or at the C−S interface, for example, in nanoparticle tagging systems,[16,49] the Au@SiO_2 NPs residing at the left of the white line (Figure 4a) are not appropriate because $E_{C-SI} < E_{S-MI}$. The set of Au@SiO_2 NPs with shell thicknesses larger than that determined from eq 8, residing at the right side of the white line, would be most appropriate for these applications because the NEF maxima are located at the C−S interface (inside the silica shell). As can be noticed from Figure 4, the intensity of the E_{C-SI} could be up to five times the intensity of E_{S-MI}, as for an NP of R_C = 17 nm and t_S = 50 nm. In general, the relative intensity of E_{C-SI} increases with the increase in shell thickness and decreases with the increase in core radius. Doering and Nie fabricated Au@SiO_2 NPs of R_C = 30 nm with t_S in between 10 and 50 nm for enhancing Raman signals of organic dyes embedded in the silica shells up to 10^{14} times to use them as Raman reports for spectroscopic tagging of DNA molecules.[16]

As can be noted from Figure 4a and eq 8, the shell thickness for which $E_{C-SI} = E_{S-MI}$ is proportional to the core radius. This is expected because the electric field intensity due to plasmonic metal NPs increases with their size,[24] and the boundary condition (eqs 6 and 7) must be fulfilled. Tian et al.[25] compared the average surface enhancement factors (ASEF) of a single Au@SiO_2 NP of 60 nm core radius with the one of 22.5 nm core radius, both with a thin silica shell of 4 nm of thickness, revealing that the ASEF (for pyridine molecule detection) of the bigger core NP is about 24 times higher than that of smaller core one due to its higher NEF at the S−M interface.[26a] To compare their results with our calculations, we extended the NEF calculation to an NP with R_C = 60 nm and t_S = 4 nm, resulting in E_{S-MI}/E_0 = 6.1, for which the estimated Raman signal enhancement was 448 (approximate enhancement factor = $|E|^4/|E_0|^4$).[24] This enhancement factor is about three times larger than the one computed for an NP with R_C = 22.5 nm and t_S = 4 nm, which is 1677, but eight times lower than the value reported by Tian et al. However, a direct comparison between the experimental result obtained by Tian et al. and our theoretical estimation is not possible because they placed the composite NPs over a silver surface, which increases the intensity of the NEF due to the secondary hotspots generated between the NPs and the metal surface. Additionally, the NPs used by Tian et al. were of quasi spherical shape with sharp edges, which also increase the intensity of the metal-core hotspots.

To verify the effect of particle size in NEF distribution, Raman spectra of R6G in aqueous solution (1 mM) were recorded again over three substrates: bare silicon as reference (curve a of Figure 6), Au_50 (layer of Au NPs of 50 nm in size; curve b, Figure 6), and Au_75 (layer of Au NPs of 75 nm in size; curve c, Figure 6). The bands in the three Raman spectra correspond to the vibrational modes of R6G in aqueous solution (see Table 1). We can see an enhancement in Raman signal for the Au_50 substrate with respect to silicon substrate

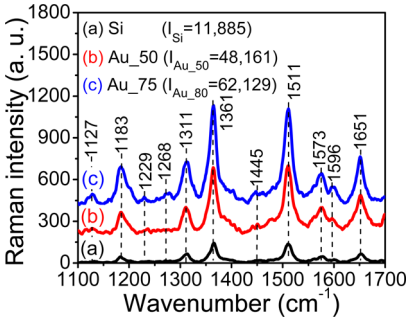

Figure 6. Raman spectra of R6G (1 mM) in aqueous solution recorded over silicon (curve a), Au_50 (curve b), and Au_75 (curve c) substrates. Labeled bands correspond to the vibrational modes of R6G (see Table 1).

DOI: 10.1021/acs.jpcc.7b07395
J. Phys. Chem. C 2017, 121, 23062−23071

($I_{Au\_50}/I_{Si} \cong 4.1$, Figure 6a,b). Nevertheless, the enhancement is more pronounced for the Au_75 substrate (curve c, Figure 6) compared with the Au_50 substrate ($I_{Au\_75}/I_{Au\_50} \cong 1.3$ or 30% more than in the Au_50 sample).

On dispersing the Au@SiO_2 NPs in water (Figure 4b), that is, in a solution with dielectric constant closer to the dielectric constant of the shell matrix, the number of composite NPs with $E_{C-SI} < E_{S-MI}$ is reduced (particles at the left of the white line in Figure 4b), whereas the number of NPs with $E_{C-SI} > E_{S-MI}$ is increased (particles at the right of the white line in Figure 4b), and the intensity of E_{C-SI} of the latter set increased up to eight times the intensity of E_{S-MI} (see Figure S7 in the Supporting Information for an Ag@SiO_2 NP). The demarcation line, for which $E_{C-SI} = E_{S-MI}$ follows the relation $t_S = 0.07R_C$ (eq S2 for an Ag@SiO_2 NP, Supporting Information).

The effect of dispersion medium is more pronounced when the dielectric constant of the medium is equal or very close to that of the shell matrix, as is the case for the Au@SiO_2 NPs dispersed in DMSO (Figure 4c). There are no composite NPs with $E_{C-SI}/E_{S-MI} \leq 1$; that is, E_{C-SI} is always higher than E_{S-MI} (up to nine times, as for an NP with R_C = 14 nm and t_S = 50 nm). Thus the NEF at the C−S interface (E_{C-SI}) is more intense when the nanoparticles are dispersed in DMSO than in a medium with lower refractive index, such as air or water (Figure 4d). For instance, the intensity of E_{C-SI} for an Au@SiO_2 NP with R_C = 30 nm and t_S = 5 nm (dotted vertical line in Figure 4d) immersed in DMSO is 1.3 times higher than the same when dispersed in water, and 3.3 times higher than the composite particle dispersed in air. Although there are no experimental reports in the literature to verify the results obtained for an NP of R_C = 30 nm and t_S = 5 nm, we estimate (from the maximum NEF, E_{S-MI}, see the dashed black line in Figure 4d) an approximated SERS enhancement factor ($|\mathbf{E}|^4/|\mathbf{E}_0|^4$)[24] of ∼714 when the particle is immersed in air, or used after soaking in analyte solution followed by a drying process. However, when the NP is soaked in water- or DMSO-based analyte solutions, the enhancement factor increases to 2809 (∼4 times larger than in air) and 3995 (∼6 times larger than in air), respectively, because the electric field at the S−M interface (E_{S-MI}) is proportional to the refractive index of the medium. The intensity of E_{S-MI} is also higher when the NP is immersed in DMSO than in water or air (1.1 and 1.5 times, respectively) for the NP of R_C = 30 nm and t_S = 5 nm. On the contrary, the intensity of E_{S-MI} for composite particles with thicker silica shell (t_S > 15 nm in the case of R_C = 30 nm, Figure 4d) is slightly higher when they are dispersed in air because the impedance mismatch between the silica shell and air is higher than in the other surrounding media, and there is little (or null) contribution of the evanescent electric field generated by the metal-core plasmon.

To verify the effect of dispersion medium on the electric field distributions around C−S and S-M interfaces, Raman spectra of R6G dissolved in water (curve a, Figure 7) and in DMSO (curve b, Figure 7) in 1 mM concentration were recorded using the Au@SiO_2_10 substrate. As can be observed in Figure 7, the Raman spectra revealed same vibrational modes of R6G for both aqueous and DMSO solution, as detected in the previous experiments (Table 1).

However, the bands revealed for the R6G in DMSO are slightly red-shifted due to the effect of surrounding medium on the vibrational frequencies.[50] Because the band appearing around 1420 cm^{-1} is associated with CH_3 degenerate deformation mode of DMSO,[51] it was intentionally suppressed

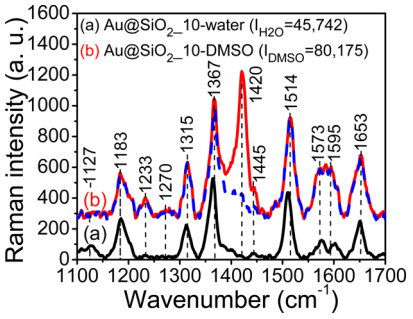

Figure 7. Raman spectra of R6G (1 mM) aqueous (curve a) and DMSO (curve b) solutions supported over Au@SiO_2_10 substrate. Labeled bands correspond to the vibrational modes of R6G (see Table 1), with the exception of the peak located at 1420 cm^{-1}, which corresponds to DMSO. The dashed spectrum presented in blue color is the spectrum subtracting the DMSO band.

from the Raman spectrum (see blue dashed line, Figure 7) to calculate the integral intensity of the SERS signal. As we can notice, the enhancement of the Raman signal is higher when the refractive index of the dispersion medium approaches the refractive index of the shell matrix. The enhancement is ∼1.8 times higher ($I_{DMSO}/I_{H_2O} \cong 1.75$) for DMSO in comparison with water, confirming the prediction drowns from our theoretical calculations. The SERS spectra Au@SiO_2_10-water and Au@SiO_2_10-DMSO have also been compared with the Raman spectra of R6G in water and DMSO using bare silicon as reference (Figures S8 and S9, Supporting Information), obtaining results qualitatively in accordance with the results predicted theoretically. Because the purpose of the present work is to design plasmonic metal@dielectric core−shell nanoparticles of optimum geometries, most suitable for SERS and fluorescence enhancement applications, we used R6G as test analyte and a 632.8 nm line of a He−Ne laser as excitation for the verification of the predictions made through theoretical calculations qualitatively. As can be noticed, the experimental results obtained using R6G as test analyte qualitatively agree well with all of the predictions made by our theoretical calculations. We believe that the use of other analytes with lower fluorescence emission in the considered spectral range of Raman signal and an excitation close to the λ_{NEF} of the plasmonic substrate would provide a higher Raman signal, producing SERS enhancement close to the theoretically predicted values.

In the case of plasmon-enhanced fluorescence application, where the fluorophores reside inside the shell matrix, we need to consider the enhancement of electric field at the C−S interface (E_{C-SI}). Again, for an NP of R_C = 30 nm and t_S = 5 nm (see the dashed black line in Figure 4d) immersed in DMSO (or water), the estimate field enhancement is about 2.5 times higher than when it is immersed in air. This effect is governed from the increase in E_{C-SI} as a consequence of stronger illumination of metal core (more light reaching the metal core) and weaker reflection (less light reflected) from the S−M interface, as described previously. Therefore, it is better to disperse the metal@dielectric NPs (or the analyte) in a solvent of refractive index closer to that of the shell matrix to increase their enhancement ability in both the surface-enhanced spectroscopies and plasmon-enhanced fluorescence applications.

The performance of these plasmonic core−shell nanostructures in SERS and PEF applications not only depends on the

DOI: 10.1021/acs.jpcc.7b07395
J. Phys. Chem. C 2017, 121, 23062−23071

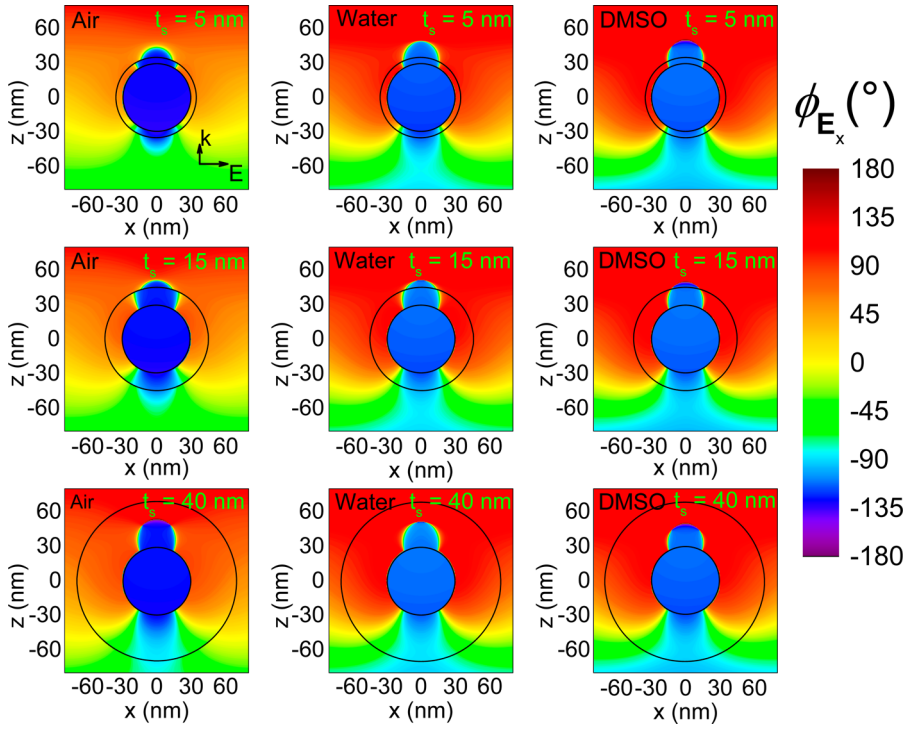

Figure 8. Near-electric-field phase (ϕ_E) maps in the $x-z$ plane (at $y = 0$) for an Au@SiO_2 NP of 30 nm core radius and 5, 15, and 40 nm of shell thicknesses, immersed in air, water, and DMSO. The excitation wavelength corresponds to λ_{NEF}.

NEF intensity at their interfaces but also on other factors like the spatial distribution of the NEF phase (ϕ_{E_x}). Hence, we calculated the ϕ_{E_x} distribution in the xz-plane (at $y = 0$) for Au@SiO_2 NPs of R_C = 30 nm with t_S= 5, 15, and 40 nm, dispersed in different media under excitation at λ_{NEF} (configurations shown in Figure 3). As can be seen from Figure 8 (Figure S10 of the Supporting Information for the NEF phase of an Ag@SiO_2 NP), irrespective of shell thickness and dispersion medium, there is no significant variation of ϕ_{E_x} in the shell or at the S−M interface along the E-polarized direction (x-axis), where the $|\mathbf{E}|/|\mathbf{E}_0|$ maximum is located (Figure 3), in any case. Additionally, the phase of the electric field inside the core suffers a phase retardation of ∼180° with respect to the shell due to the retardation effect of the conduction electrons.[24]

Such a uniform NEF phase distribution throughout the shell matrix and its surrounding will also maintain the original phase of the radiations coming from the fluorophores and tagging molecules embedded in silica matrix along the x-axis without affecting their enhancement (plasmon enhancement) due to destructive interference. However, the retardation effect of the NEF inside the metal core is extended through the silica shell (and even in the dielectric media for thin silica shells) in the direction parallel to the propagation vector (k, along the z-axis), which might cause a destructive superposition of the radiation emitted by the fluorophores and the exciting radiation.

Therefore, the fluorescence of fluorophores or dyes located along the x-direction not only will be enhanced by the plasmonic core but also will not be quenched due to the phase retardation as for the fluorophores located at the z-direction (and y-direction, not shown here).

4. CONCLUSIONS

We have demonstrated the possibility of designing metal@dielectric core−shell NPs locating the maximum of NEF either at the C−S interface or at the S−M interface, depending on their dimensions and the difference between the dielectric constants of the shell material and the surrounding medium. Optimal response of these plasmonic composite particles in plasmon-enhanced systems (SERS and PEF) can only be obtained if their geometrical parameters such as core radius and shell thickness are carefully engineered prior to synthesis. Au@SiO_2/Ag@SiO_2 NPs of optimal geometrical dimensions (R_C and t_S) are the best options for using them in surface-enhanced spectroscopies or in plasmon-enhanced fluorescence systems, whereas they are dispersed in common medium such as air, water, or DMSO. Through theoretical calculations and experimental verifications, we confirm that it is better to disperse the analytes in a solvent of refractive index close to the refractive index of the shell material to increase the signal enhancement response in SERS (in assay systems, for instance). This also applies to plasmon-enhanced fluorescence systems, where the fluorophores are located inside the shell or anchored with it.

■ ASSOCIATED CONTENT

Supporting Information

The Supporting Information is available free of charge on the ACS Publications website at DOI: 10.1021/acs.jpcc.7b07395.

Size distribution histograms of synthesized Au NPs and Au@SiO_2. Enhanced electric field at the core−shell and shell−medium interfaces as a function of the wavelength for a Au@SiO_2 NP and Ag@ SiO_2 NP of 30 nm core radius and 5, 15, and 40 nm of shell thickness, immersed in air, water, and DMSO. $|\mathbf{E}|/|\mathbf{E}_0|$ color maps in the xz-plane of a Ag@SiO_2 NP of R_C = 30 nm and t_S = 5, 15,

DOI: 10.1021/acs.jpcc.7b07395
J. Phys. Chem. C 2017, 121, 23062−23071

and 40 nm, surrounded by air, water, and DMSO. $|\mathbf{E}|/|\mathbf{E}_0|$ along the *x*-direction for an Au@SiO_2 NP and Ag@SiO_2 NP R_C = 30 nm and t_S = 5, 15, and 40 nm, immersed in air, water, and DMSO. Color maps of E_{C-SI}/E_{S-MI} for a Ag@SiO_2 NP as a function of the dimensions of the core (*y*-axis) and shell (*x*-axis) and for the three surrounding media: air, water, and DMSO. Linear relation equations between Ag core radius and silica shell thickness in which $E_{C-MI} = E_{S-MI}$ in air and water for the dipolar mode. Raman spectra of R6G in aqueous and DMSO solution recorded over silicon and Au@SiO_2_10 substrates. NEF phase maps on the *xz*-plane for an Ag@SiO2 NP of R_C = 30 nm and t_S = 5, 15, and 40 nm, immersed in air, water, and DMSO. (PDF)

AUTHOR INFORMATION

Corresponding Author

*E-mail: upal@ifuap.buap.mx. Fax: +52-222-2295611.

ORCID

Ovidio Peña-Rodríguez: 0000-0002-7329-0550

Umapada Pal: 0000-0002-5665-106X

Author Contributions

All authors have given approval to the final version of the manuscript.

Notes

The authors declare no competing financial interest.

ACKNOWLEDGMENTS

The work was financially supported by DITCo and VIEP, BUAP (Grant no. VIEP/EXC/2017-257). J.L.M.-P. acknowledges CONACyT, Mexico, for offering doctoral fellowship. We acknowledge the computational and technical support extended by Laboratorio Nacional de Supercómputo del Sureste de México (Grant no. F-018C).

REFERENCES

(1) Where now for plasmonics? *Nat. Nanotechnol.* **2016**, *11*, 1.

(2) Petryayeva, E.; Krull, U. J. Localized Surface Plasmon Resonance: Nanostructures, Bioassays and Biosensing-A Review. *Anal. Chim. Acta* **2011**, *706*, 8−24.

(3) Stockman, M. I. Nanoplasmonics: Past, Present, and Glimpse Into Future. *Opt. Express* **2011**, *19*, 22029−22106.

(4) Atwater, H. A.; Polman, A. Plasmonics for Improved Photovoltaic Devices. *Nat. Mater.* **2010**, *9*, 205−213.

(5) Lakowicz, J. R. Radiative Decay Engineering: Biophysical and Biomedical Applications. *Anal. Biochem.* **2001**, *298*, 1−24.

(6) Aslan, K.; Pérez-Luna, V. H. Quenched Emission of Fluorescence by Ligand Functionalized Gold Nanoparticles. *J. Fluoresc.* **2004**, *14*, 401−405.

(7) Willets, K. A.; van Duyne, R. P. Localized Surface Plasmon Resonance Spectroscopy and Sensing. *Annu. Rev. Phys. Chem.* **2007**, *58*, 267−297.

(8) Álvarez-Puebla, R. A. Effects of the Excitation Wavelength on the SERS Spectrum. *J. Phys. Chem. Lett.* **2012**, *3*, 857−866.

(9) Li, J. F.; Huang, Y. F.; Ding, Y.; Yang, Z. L.; Li, S. B.; Zhou, X. S.; Fan, F. R.; Zhang, W.; Zhou, Z. Y.; Wu, D. Y.; Ren, B.; Wang, Z. L.; Tian, Z. Q. Shell-Isolated Nanoparticle-Enhanced Raman Spectroscopy. *Nature* **2010**, *464*, 392−395.

(10) Tcherniak, A.; Ha, J. W.; Dominguez-Medina, S.; Slaughter, L. S.; Link, S. Probing a Century Old Prediction One Plasmonic Particle at a Time. *Nano Lett.* **2010**, *10*, 1398−1404.

(11) Jang, L.-W.; Jeon, D.-W.; Kim, M.; Jeon, J.-W.; Polyakov, A. Y.; Ju, J.-W.; Lee, S.-J.; Baek, J.-H.; Yang, J.-K.; Lee, I.-H. Investigation of Optical and Structural Stability of Localized Surface Plasmon Mediated Light-Emitting Diodes by Ag and Ag/SiO_2 Nanoparticles. *Adv. Funct. Mater.* **2012**, *22*, 2728−2734.

(12) Cerruti, M. G.; Sauthier, M.; Leonard, D.; Liu, D.; Duscher, G.; Feldheim, D. L.; Franzen, S. Gold and Silica-Coated Gold Nanoparticles as Thermographic Labels for DNA Detection. *Anal. Chem.* **2006**, *78*, 3282−3288.

(13) Standridge, S. D.; Schatz, G. C.; Hupp, J. T. Distance Dependence of Plasmon-Enhanced Photocurrent in Dye-Sensitized Solar Cells. *J. Am. Chem. Soc.* **2009**, *131*, 8407−8409.

(14) Qi, J.; Dang, X.; Hammond, P. T.; Belcher, A. M. Highly Efficient Plasmon-Enhanced Dye-Sensitized Solar Cells through Metal@Oxide Core Shell Nanostructure. *ACS Nano* **2011**, *5*, 7108−7116.

(15) Wu, J.-L.; Chen, F.-C.; Hsiao, Y.-S.; Chien, F.-C.; Chen, P.; Kuo, C.-H.; Huang, M. H.; Hsu, C.-S. Surface Plasmonic Effects of Metallic Nanoparticles on the Performance of Polymer Bulk Heterojunction Solar Cells. *ACS Nano* **2011**, *5*, 959−967.

(16) Doering, W. E.; Nie, S. Spectroscopic Tags Using Dye-Embedded Nanoparticles and Surface-Enhanced Raman Scattering. *Anal. Chem.* **2003**, *75*, 6171−6176.

(17) Kong, X.; Yu, Q.; Zhang, X.; Du, X.; Gong, H.; Jiang, H. Synthesis and Application of Surface Enhanced Raman Scattering (SERS) Tags Of Ag@SiO_2 Core/Shell Nanoparticles in Protein Detection. *J. Mater. Chem.* **2012**, *22*, 7767−7774.

(18) Asselin, J.; Legros, P.; Grégoire, A.; Boudreau, D. Correlating Metal-Enhanced Fluorescence and Structural Properties in Ag@SiO_2 Core-Shell Nanoparticles. *Plasmonics* **2016**, *11*, 1369−1376.

(19) Chen, J.; Jin, Y.; Fahruddin, N.; Zhao, J. X. Development of Gold Nanoparticle-Enhanced Fluorescent Nanocomposites. *Langmuir* **2013**, *29*, 1584−1591.

(20) Park, Y.-S.; Kasuya, A.; Dmytruk, A.; Yasuto, N.; Takeda, M.; Ohuchi, N.; Sato, Y.; Tohji, K.; Uo, M.; Watari, F. Concentrated Colloids of Silica-Encapsulated Gold Nanoparticles: Colloidal Stability, Cytotoxicity, and X-ray Absorption. *J. Nanosci. Nanotechnol.* **2007**, *7*, 2690−2695.

(21) Kumar, C. S. S. R. *Mixed Metal Nanomaterials*; Nanomaterials for the Life Sciences 3; John Wiley & Sons, 2009; pp 332−342.

(22) Montaño-Priede, J. L.; Coelho, J. P.; Guerrero-Martínez, A.; Peña Rodríguez, O.; Pal, U. Fabrication of Monodispersed Au@SiO_2 Nanoparticles with Highly Stable Silica Layers by Ultrasound Assisted Stöber Method. *J. Phys. Chem. C* **2017**, *121*, 9543−9551.

(23) Aslan, K.; Wu, M.; Lakowicz, J. R.; Geddes, C. D. Fluorescent Core-Shell Ag@SiO_2 Nanocomposites for Metal-Enhanced Fluorescence and Single Nanoparticle Sensing Platforms. *J. Am. Chem. Soc.* **2007**, *129*, 1524−1525.

(24) Montaño-Priede, L.; Peña-Rodríguez, O.; Rivera, A.; Guerrero-Martínez, A.; Pal, U. Optimizing the Electric Field around Solid and Core−Shell Alloy Nanostructures for Near-Field Applications. *Nanoscale* **2016**, *8*, 14836−14845.

(25) Tian, X.-D.; Liu, B.-J.; Li, J.-F.; Yang, Z.-L.; Ren, B.; Tian, Z.-Q. SHINERS and Plasmonic Properties of Au Core SiO_2 Shell Nanoparticles with Optimal Core Size and Shell Thickness. *J. Raman Spectrosc.* **2013**, *44*, 994−998.

(26) (a) Anema, J. R.; Li, J.-F.; Yang, Z.-L.; Ren, B.; Tian, Z.-Q. Shell-Isolated Nanoparticle-Enhanced Raman Spectroscopy: Expanding the Versatility of Surface-Enhanced Raman Scattering. *Annu. Rev. Anal. Chem.* **2011**, *4*, 129−150. (b) Shanthil, M.; Thomas, R.; Swathi, R. S.; Thomas, K. G. Ag@SiO2 Core−Shell Nanostructures: Distance-Dependent Plasmon Coupling and SERS Investigation. *J. Phys. Chem. Lett.* **2012**, *3*, 1459−1464.

(27) Fang, P.-P.; Li, J.-F.; Yang, Z.-L.; Li, L.-M.; Ren, B.; Tian, Z.-Q. Optimization of SERS Activities of Gold Nanoparticles and Gold-Core−Palladium-Shell Nanoparticles by Controlling Size and Shell Thickness. *J. Raman Spectrosc.* **2008**, *39*, 1679−1687.

(28) Ladutenko, K.; Pal, U.; Rivera, A.; Peña-Rodríguez, O. Mie Calculation of Electromagnetic Near-Field for a Multilayered Sphere. *Comput. Phys. Commun.* **2017**, *214*, 225−230.

(29) Bohren, C. F.; Huffman, D. R. *Absorption and Scattering of Light by Small Particles*; Wiley-Interscience: Weinheim, Germany, 1998.

DOI: 10.1021/acs.jpcc.7b07395
J. Phys. Chem. C 2017, 121, 23062−23071

(30) Penndorf, R. Tables of the Refractive Index for Standard Air and the Rayleigh Scattering Coefficient for the Spectral Region between 0.2 and 20.0 um and Their Application to Atmospheric Optics. *J. Opt. Soc. Am.* **1957**, *47*, 176−182.
(31) Thormählen, I.; Straub, J.; Grigull, U. Refractive Index of Water and Its Dependences on Wavelength, Temperature, and Density. *J. Phys. Chem. Ref. Data* **1985**, *14*, 933−945.
(32) Aminabhavi, T. M.; Gopalakrishna, B. Density, Viscosity, Refractive Index, and Speed of Sound in Aqueous Mixtures of N,N-Dimethylformamide, Dimethyl Sulfoxide, N,N-Dimethylacetamide, Acetonitrile, Ethylene Glycol, Diethylene Glycol, 1,4-Dioxane, Tetrahydrofuran, 2-Methoxyethanol, and 2-Ethoxyethanol at 298.15 K. *J. Chem. Eng. Data* **1995**, *40*, 856−861.
(33) Link, S.; El-Sayed, M. A. Size and Temperature Dependence of the Plasmon Absorption of Colloidal Gold Nanoparticles. *J. Phys. Chem. B* **1999**, *103*, 4212−4217.
(34) Peña-Rodríguez, O.; Caro, M.; Rivera, A.; Olivares, J.; Perlado, J. M.; Caro, A. Optical Properties of Au-Ag Alloys: An Ellipsometric Study. *Opt. Mater. Express* **2014**, *4*, 403−410.
(35) Malitson, I. H. Interspecimen Comparison of the Refractive Index of Fused Silica. *J. Opt. Soc. Am.* **1965**, *55*, 1205−1209.
(36) Sugden, M. W.; Richardson, T. H.; Leggett, G. Sub-10 Ω Resistance Gold Films Prepared by Removal of Ligands from Thiol-Stabilized 6 nm Gold Nanoparticles. *Langmuir* **2010**, *26*, 4331−4338.
(37) Kim, K.-H.; Park, Q.-H. Perfect Anti-Reflection from First Principles. *Sci. Rep.* **2013**, *3* (1062), 1−5.
(38) Kelly, K. L.; Coronado, E.; Zhao, L. L.; Schatz, G. C. The Optical Properties of Metal Nanoparticles: The Influence of Size, Shape, and Dielectric Environment. *J. Phys. Chem. B* **2003**, *107*, 668−677.
(39) Moores, A.; Goettmann, F. The Plasmon Band in Noble Metal Nanoparticles: An Introduction to Theory and Applications. *New J. Chem.* **2006**, *30*, 1121−1132.
(40) Zhang, D.; Cherkaev, E.; Lamoureux, M. P. Stieltjes Representation of the 3D Bruggeman Effective Medium and Padé Approximation. *Appl. Math. Comput.* **2011**, *217*, 7092−7107.
(41) Liu, X.; Li, D.; Sun, X.; Li, Z.; Song, H.; Jiang, H.; Chen, Y. Tunable Dipole Surface Plasmon Resonances of Silver Nanoparticles by Cladding Dielectric Layers. *Sci. Rep.* **2015**, *5* (1), 1−7.
(42) Gutierrez, Y.; Ortiz, D.; Sanz, J. M.; Saiz, J. M.; Gonzalez, F.; Everitt, H. O.; Moreno, F. How an Oxide Shell Affects the Ultraviolet Plasmonic Behavior of Ga, Mg, and Al Nanostructures. *Opt. Express* **2016**, *24*, 20621−20631.
(43) Jain, P. K.; Huang, X.; El-Sayed, I. H.; El-Sayed, M. A. Review of Some Interesting Surface Plasmon Resonance-enhanced Properties of Noble Metal Nanoparticles and Their Applications to Biosystems. *Plasmonics* **2007**, *2*, 107−118.
(44) Chandra, S.; Doran, J.; McCormack, S. J.; Kennedy, M.; Chatten, A. J. Enhanced Quantum Dot Emission for Luminescent Solar Concentrators Using Plasmonic Interaction. *Sol. Energy Mater. Sol. Cells* **2012**, *98*, 385−390.
(45) Kochuveedu, S. T.; Son, T.; Lee, Y.; Lee, M.; Kim, D.; Kim, D. H. Revolutionizing the FRET-Based Light Emission in Core-Shell Nanostructures via Comprehensive Activity of Surface Plasmons. *Sci. Rep.* **2015**, *4* (1), 1−8.
(46) Li, G.; Li, H.; Mo, Y.; Huang, X.; Chen, L. Surface enhanced resonance Raman spectroscopy of rhodamine 6G adsorbed on silver electrode in lithium batteries. *Chem. Phys. Lett.* **2000**, *330*, 249−254.
(47) Cyriac, J.; Wleklinski, M.; Li, G.; Gao, L.; Cooks, R. G. In situ Raman spectroscopy of surfaces modified by ion soft landing. *Analyst* **2012**, *137*, 1363−1369.
(48) Vančo, Ľ.; Kadlečíková, M.; Breza, J.; Vojs, M.; Michniak, P.; Marton, M. Interference enhancement in SERS spectra of rhodamine 6G: Relation to reflectance. *Vib. Spectrosc.* **2017**, *90*, 31−37.
(49) Mulvaney, S. P.; Musick, M. D.; Keating, C. D.; Natan, M. J. Glass-Coated, Analyte-Tagged Nanoparticles: A New Tagging System Based on Detection with Surface-Enhanced Raman Scattering. *Langmuir* **2003**, *19*, 4784−4790.
(50) Montagna, M.; Dusi, R. Raman scattering from small spherical particles. *Phys. Rev. B: Condens. Matter Mater. Phys.* **1995**, *52*, 10080−10089.
(51) Selvarajan, A. Raman Spectrum of Dimethyl Sulfoxide (DMSO) and the Influence of Solvents. *Proc. - Indian Acad. Sci., Sect. A* **1966**, *64*, 44−50.

DOI: 10.1021/acs.jpcc.7b07395
J. Phys. Chem. C 2017, 121, 23062−23071